On the inference of ERK signaling dynamics from protein biosensor measurements

Shah Md. Toufiqur Rahman and Jason M. Haugh*
Department of Chemical and Biomolecular Engineering, North Carolina State University, Raleigh, NC 27606

ABSTRACT **The extracellular signal-regulated kinase (ERK) signaling pathway plays prominent roles in cell growth, proliferation, and differentiation. ERK signaling is dynamic, involving phosphorylation/dephosphorylation, nucleocytoplasmic shuttling, and interactions with scores of protein substrates in the cytosol and in the nucleus. Live-cell fluorescence microscopy using genetically encoded ERK biosensors offers the potential to infer those dynamics in individual cells. In this study, we have monitored ERK signaling using four commonly used translocation- and Förster resonance energy transfer-based biosensors in a common cell stimulation context. Consistent with previous reports, we found that each biosensor responds with unique kinetics; it is clear that there is not a single dynamic signature characterizing the complexity of ERK phosphorylation, translocation, and kinase activity. In particular, the widely adopted ERK Kinase Translocation Reporter (ERKKTR) gives a readout that reflects ERK activity in both compartments. Mathematical modeling offers an interpretation of the measured ERKKTR kinetics, in relation to cytosolic and nuclear ERK activity, and suggests that biosensor-specific dynamics substantially influence the measured output.**

Monitoring Editor
Diane Lidke
University of New Mexico

Received: Nov 3, 2022
Revised: Feb 3, 2023
Accepted: Feb 27, 2023

INTRODUCTION

Extracellular signal-regulated kinases 1 and 2 (hereafter, ERK1/2) are serine-threonine kinases of the mitogen-activated protein kinase (MAPK) family that are considered master regulators of cell growth, proliferation, and differentiation in metazoans (Zhang and Liu, 2002; Mebratu and Tesfaigzi, 2009; Schevzov *et al.*, 2015), and dysregulation of ERK1/2 signaling has been implicated in the progression of most cancers (Kohno and Pouyssegur, 2006; McCubrey *et al.*, 2007; Roberts and Der, 2007). ERK1/2 and other MAPKs are the last protein kinases to be activated by sequential phosphorylation in canonical, three-kinase cascades that respond to growth factor stimulation or/and stress signals (Seger and Krebs, 1995; Garrington and Johnson, 1999; Chang and Karin, 2001; Zhang and Liu, 2002). To assess the dynamics of ERK1/2 and other signaling dynamics, various biochemical approaches may be employed to quantify the phosphorylation states of key signaling proteins at discrete time points after cell stimulation; however, this approach generally has poor temporal resolution, offers limited information about subcellular localization, and reports only an aggregate snapshot of a cell population. Live-cell imaging with fluorescent protein (FP)-tagged proteins/biosensors provides more precise spatial and temporal information about signal transduction (Zacharias *et al.*, 2000; Hahn and Toutchkine, 2002, Gaits and Hahn, 2003; Meyer and Teruel, 2003; Chavez-Abiega *et al.*, 2019).

Spurred by the biological and biomedical relevance of ERK1/2 signaling, various live-cell fluorescence strategies have been developed to continuously monitor the pathway in single cells. The first strategy was to fuse ERK1 or ERK2 with enhanced green FP (or other FPs) and track its translocation from the cytosol to the nucleus, a hallmark of ERK1/2 activation (Yung *et al.*, 2001). With this approach, either transient or sustained translocation dynamics have been observed, depending on the stimulus and experimental model system (Ebisuya *et al.*, 2005; Sasagawa *et al.*, 2005; Ahmed *et al.*, 2014). Sustained oscillations of ERK nucleocytoplasmic shuttling have been observed under certain conditions (Shankaran *et al.*, 2009). To measure the enzymatic activity of ERK1/2 more directly, Förster resonance energy transfer (FRET)-based biosensors reporting ERK1/2 kinase activity have also been developed and with

This article was published online ahead of print in MBoC in Press (http://www.molbiolcell.org/cgi/doi/10.1091/mbc.E22-10-0476) on March 8, 2023.

*Address correspondence to: Jason M. Haugh (jason_haugh@ncsu.edu).

Abbreviations used: bNLS, bipartite nuclear localization signal; EC, export complex; ERK, extracellular signal-regulated kinase; ERKKTR, ERK Kinase Translocation Reporter; FP, fluorescent protein; FRET, Förster resonance energy transfer; IC, import complex; MAPK, mitogen-activated protein kinase; NES, nuclear export signal; NPC, nuclear pore complex; PDGF, platelet-derived growth factor-BB; TFP, teal fluorescent protein.

nuclear export/import sequences added to report on ERK1/2 activity in the cytosol/nucleus, respectively (cyto- and nuc-EKAR) (Harvey *et al.*, 2008). Combining biochemical measurements and live-cell imaging results from mouse fibroblast NIH 3T3 cells using the FP-tagged ERK1/2 and cyto- and nuc-EKAR biosensors, our laboratory developed a data-driven kinetic model of growth factor-stimulated ERK signaling (Ahmed *et al.*, 2014). This model explains how phosphorylation and total nuclear ERK1/2 can show dramatic adaptation, while the enzymatic activities of ERK1/2 in the cytosol and nucleus do not. In particular, nuclear ERK1/2 activity accumulates slowly, reaching a plateau well after the peak in total nuclear ERK1/2 in the same cell. The transient nature of whole-cell ERK1/2 phosphorylation is consistent with high-affinity interactions of phosphorylated ERK1/2 with one or more of its protein substrates, which had also been inferred from quasi-steady-state measurements in *Drosophila* embryos (Kim *et al.*, 2011; Lee *et al.*, 2019).

More recently, the ERK Kinase Translocation Reporter (ERKKTR) was developed (Regot *et al.*, 2014; Kudo *et al.*, 2018). In this biosensor, the docking sites of the ERK1/2 substrate Elk1 are conjugated with a bipartite nuclear localization signal (bNLS) and nuclear export signal (NES). The bNLS is neutralized when phosphorylated by ERK1/2, whereas the NES is activated when phosphorylated by ERK1/2; thus, ERKKTR translocates from the nucleus to the cytosol in the presence of active ERK1/2. The simplicity and high signal-to-noise ratio of the ERKKTR measurement make this biosensor an attractive alternative to the FRET-based biosensors (Kudo *et al.*, 2018). However, the readout obtained with ERKKTR might be difficult to interpret, because it can be phosphorylated by ERK1/2 while either in the nucleus or in the cytosol. We have addressed this question by combining newly and previously acquired kinetic data with an updated mathematical model that accounts for ERKKTR dynamics. In the context of growth factor-stimulated fibroblasts, the data show that ERKKTR misses the initial cytosolic ERK1/2 activity dynamics and also the slow accumulation of nuclear ERK1/2 activity. The model-guided interpretation is that the initial translocation of ERKKTR is frustrated by the biosensor-specific dynamics. Although ERKKTR phosphorylation in the nucleus is not likely rate-limiting, ERKKTR phosphorylated on only the NES is in a "compartment-fluid" form that is predicted to buffer the decisive translocation of the biosensor between the nucleus and cytosol. These results reveal caveats associated with the use of translocation-based biosensors to infer signaling dynamics of ERK1/2 and other protein kinases.

RESULTS

Measurements of ERK1/2 signaling dynamics using available biosensors show unique kinetics

To assess ERK1/2 signaling dynamics in a common stimulation context, we transiently expressed each of the four available ERK1/2 biosensors (Figure 1A) in NIH 3T3 mouse fibroblasts. The cells were serum starved and then maximally stimulated with platelet-derived growth factor-BB (PDGF, 1 nM) while monitored by fluorescence microscopy (see Supplemental Figure S1 for representative montages). Consistent with previous results (Ahmed *et al.*, 2014), PDGF-stimulated nuclear localization of FP-tagged ERK2 is transient, peaking after ~8 min and attaining an adapted steady state after ~45 min (Figure 1B). By comparison, the FRET-based cyto- and nuc-EKAR biosensors report ERK1/2-kinase activity in the cytosol and nucleus, and they exhibit relatively fast (peak at ~6 min) and slow (plateau at ~15 min) kinetics, respectively, with little or no apparent adaptation (Figure 1, C and D). It was confirmed previously that the relatively slow nuc-EKAR response reflects the availability of active ERK1/2 in the nucleus, not intrinsically sluggish dynamics of the EKAR biosensor; with subsequent inhibition of the upstream kinase, MEK1/2, both cyto- and nuc-EKAR FRET readouts return to baseline within ~2 min (Ahmed *et al.*, 2014). Under the same stimulation conditions, the ERKKTR biosensor exhibits kinetics that are quite different from those of the other three (Figure 1E). This is also shown for cells co-expressing FP-ERK2 and ERKKTR (Supplemental Figure S2). ERKKTR translocation is initially delayed, with no detectable change for ~2 min, after which it rapidly increases, peaks at ~10 min, then steadily decreases with time. And, as we will show, decay of the ERKKTR readout following MEK1/2 inhibition is relatively slow.

The dynamic range of the ERKKTR biosensor is limited under normal ERK activation conditions

To better understand the ERKKTR response to stimulation, we sought to estimate the fractions of ERKKTR in the nucleus and cytosol and the relative rates of ERKKTR nucleocytoplasmic shuttling under serum-starved and stimulated conditions. In epifluorescence images, the identified nuclear region contains the nucleus of course, but also portions of the cytosol above and below (Figure 2A). We refer to the cytosolic fluorescence contained within the nuclear region as "spillover." From the images of cells expressing the cyto-EKAR biosensor, which contains a canonical NES (almost 100% cytosolic), we quantified the ratio of the mean fluorescence intensity in the nuclear region (attributed to spillover) to that of a surrounding ring region in the cytosol (Figure 2B). Ascribing the mean value of this fluorescence ratio to any cell image, one can approximately correct the fluorescence of the nuclear region for the cytosolic spillover and thus estimate the fractions of the whole-cell fluorescence actually contained in the cytosol and nucleus. As expected, applying this correction to the cyto-EKAR images yielded a mean cytosolic fraction close to 1, which was stable throughout a protocol of PDGF stimulation followed by addition of the MEK inhibitor, U0126 (Figure 2, C and D).

Applying this procedure to the ERKKTR images, we estimate that an average of 75% of the biosensor was in the cytosol in our serum-starved cells initially, while only 25% of the biosensor was actually inside the nucleus. Following PDGF stimulation, the cytosolic fraction of ERKKTR was estimated to peak at close to 1, i.e., with only a small fraction remaining inside the nucleus (Figure 2E). The near-complete emptying of nuclear ERKKTR in stimulated cells was confirmed by confocal microscopy (Figure 2F). We conclude that the extent of the ERKKTR translocation response was readily maxed/saturated under our normal ERK activation conditions. With the ERKKTR readout properly scaled, also presented in Figure 2E is its decay following addition of the MEK inhibitor, U0126. Relative to FP-ERK nuclear localization and the EKAR readouts, which decay with half times ~1–3 min (Ahmed *et al.*, 2014), the decay of ERKKTR translocation is much slower (see also Supplemental Figure S2). This further indicates that biosensor-specific dynamics affect the ERKKTR response kinetics.

With a predicted molecular weight of 35 kDa, ERKKTR passively diffuses through nuclear pores. Considering that MEK inhibition returns the ERKKTR response to baseline (Figure 2E), serum starvation was effective in eliminating detectable ERK activity; we reason that the localization of ERKKTR prior to stimulation is determined by the balance of passive transport across the nuclear membrane and active nuclear import promoted by the unphosphorylated bNLS. To assess the influence of the bNLS, we imaged the volume marker, teal fluorescent protein (TFP), which is distributed by passive diffusion only. Correcting fluorescence in the nuclear region as described above, we found that an average of 84% of TFP was in the cytosol (16% in the nucleus) (Supplemental Figure S3), presumably reflecting

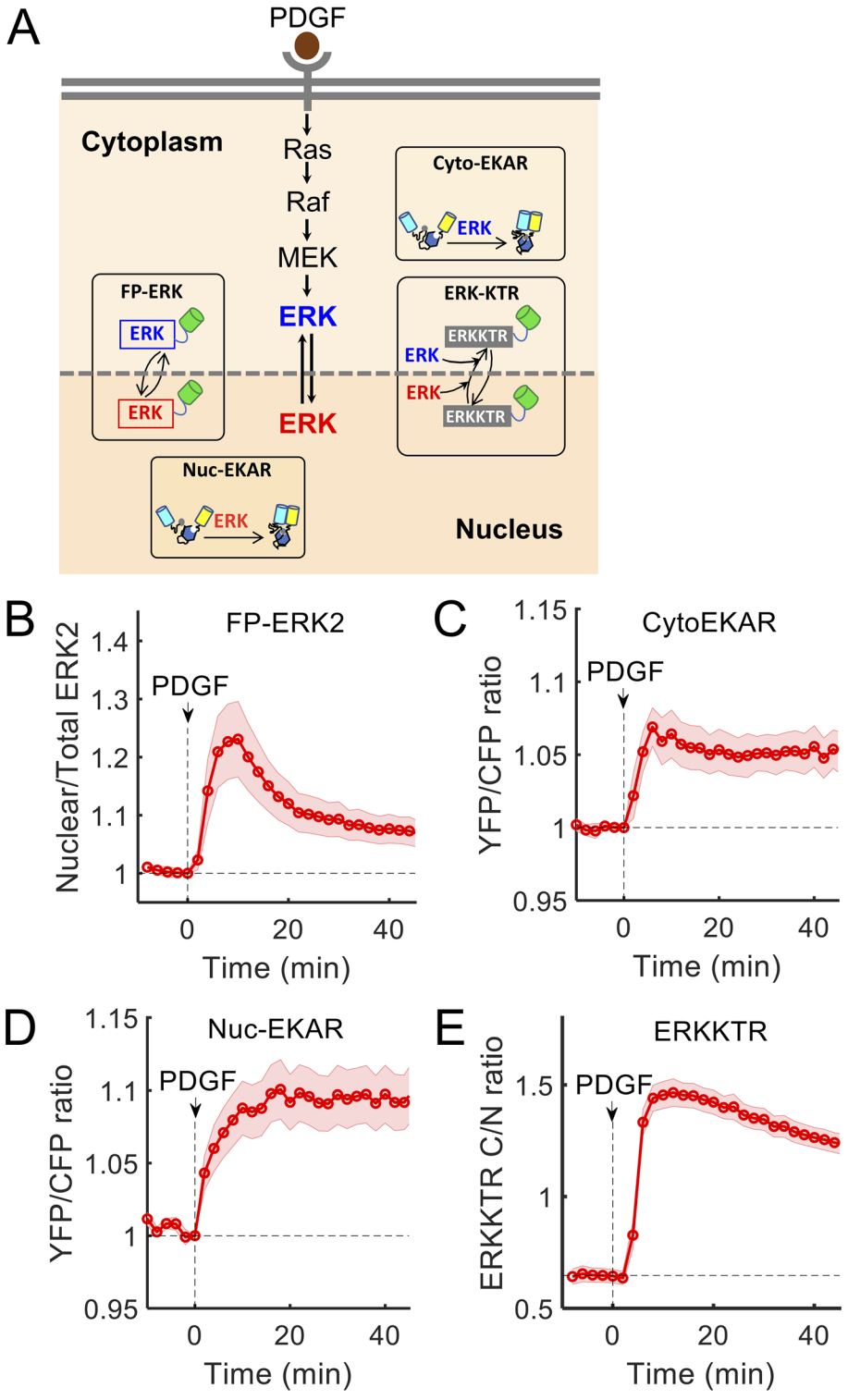

FIGURE 1: ERK activity measurements using available live-cell fluorescent reporters. (A) Schematic of PDGF-stimulated ERK-signaling cascade along with four different live-cell biosensors for probing ERK activitation. (B–E) NIH 3T3 mouse fibroblasts transiently expressing GFP-ERK2 (B, $n = 29$), cytosolic (Cyto-) EKAR (C, $n = 28$), nuclear (Nuc-) EKAR (D, $n = 30$), or ERKKTR-Clover (E, $n = 70$) were serum starved for 4 h, then stimulated with PDGF (1 nM). The symbols indicate the mean normalized readout, and the shaded regions shows the 95% confidence intervals. Each set of data was pooled from three independent experiments.

the (accessible) volumes of the two compartments. Assuming that the export of unphosphorylated ERKKTR from the nucleus, like TFP, is passive, and that net fluxes of ERKKTR and TFP across the nuclear membrane are approximately zero at steady state, we estimate that the ERKKTR bNLS increases the rate of nuclear import by approximately twofold in unstimulated cells (*Materials and Methods*). We conclude that, in the absence of ERK activity, active import of ERKKTR (due to the unphosphorylated bNLS) and passive diffusion across nuclear pores contribute about equally to the crossing of ERKKTR from the cytosol to the nucleus. This analysis provides a quantitative basis for the assessment of the ERKKTR kinetics following growth factor stimulation.

An updated model of ERK1/2 dynamics reconciles the observed ERKKTR kinetics

We have amended the previous model (Ahmed *et al.*, 2014) (Figure 3A) by adding processes that apply only to ERKKTR (Supplemental Text S1). The ERKKTR biosensor was constructed from the ERK-docking site fragment (312-356) of Elk-1 in tandem with the aforementioned bNLS and NES; the bNLS and NES each have three serine phosphorylation sites that affect nucleocytoplasmic shuttling (Regot *et al.*, 2014). Phosphorylation by ERK1/2 disrupts nuclear import and activates nuclear export. In the kinetic model proposed by Regot *et al.* (2014), it was assumed that ERKKTR is sequentially phosphorylated by ERK1/2, first at the bNLS and then at the NES (Regot *et al.*, 2014). In our present model, switching off or on of the bNLS or NES was also treated as a single phosphorylation event (meaning that either a single phosphorylation is sufficient for the switch or the sites in each of the bNLS and NES are phosphorylated processively), but these modifications are considered independent rather than sequential (Figure 3B). Phosphorylation and dephosphorylation of the bNLS and NES are allowed different, compartment-specific rate constants. Our model also considers nuclear export and import as multistep processes (Figure 3C). Forms of nuclear ERKKTR with NES phosphorylated may engage in an export complex (EC), which translocates to the cytoplasm and then releases ERKKTR. Forms of cytosolic ERKKTR with unphosphorylated bNLS may engage in an import complex (IC), which translocates to the nucleus and then releases ERKKTR. These considerations are based on energy-dependent transport of proteins with a NLS or NES (Gama-Carvalho and Carmo-Fonseca, 2001; Pemberton and Paschal, 2005; Freitas and Cunha, 2009; Kim *et al.*, 2017), for example, as driven by the Ran GTPase shuttling mechanism (Cole and Hammell, 1998; Kuersten *et al.*, 2001). In addition to the transitions depicted in Figure 3C, the model accounts for passive, nucleocytoplasmic flux

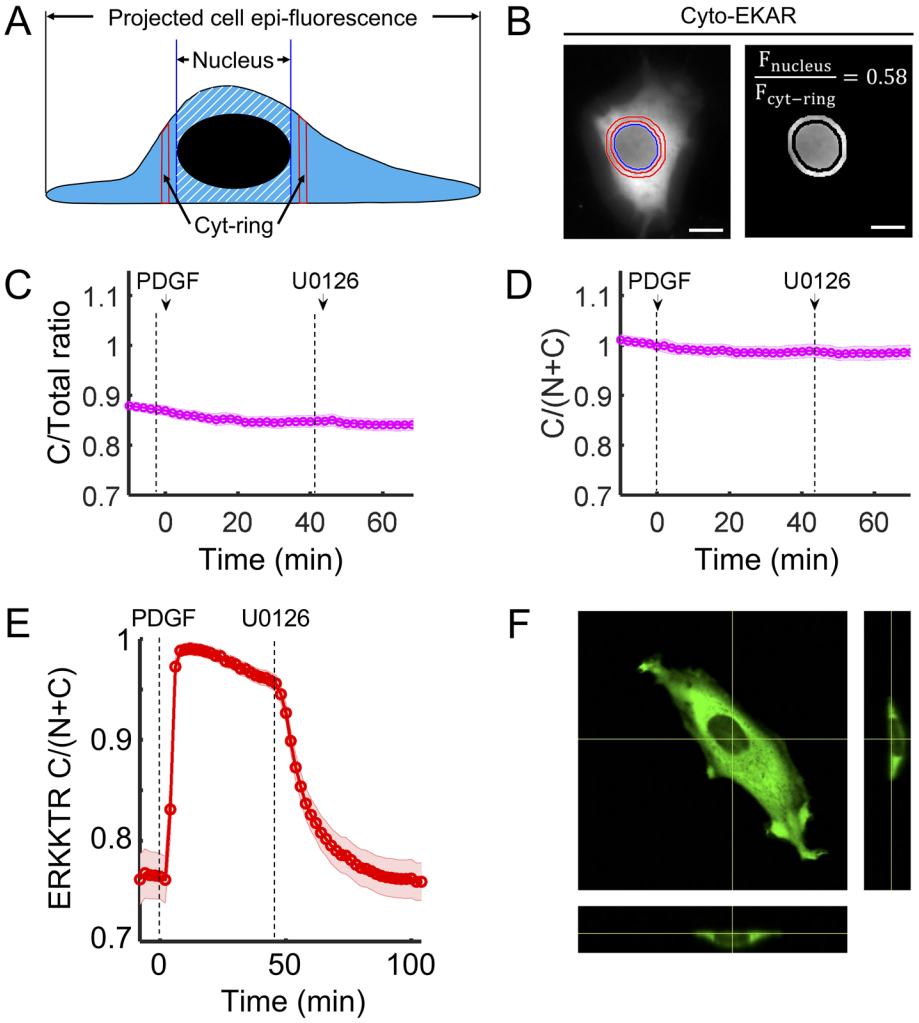

FIGURE 2: Estimation of nuclear and cytosolic fluorescence from epifluorescence images. (A) Side-view cartoon illustrating the "spillover" effect in segmented epifluorescence images. The nuclear area includes cytosolic regions above and below the nucleus (shaded). To correct for this, the mean fluorescence in a ring around the nuclear region (cyt-ring) is measured. (B) Representative images showing Cyto-EKAR biosensor in NIH 3T3 cells imaged by epifluorescence microscopy setting. Scale bar = 10 μm. The nuclear and cyto-ring (5 pixels wide and 5 pixels away from the nucleus) regions are marked with blue and red lines respectively. The mean intensity ratio of nuclear and cyt-ring fluorescence was calculated from a population of these cells. (C and D) The ratio of total cytosolic fluorescence over the total cellular fluorescence of Cyto-EKAR biosensor without (C) or with spillover correction (D) (mean ± 95% confidence interval, $n = 98$). (E) Correction of the ERKKTR data shown in Figure 1E with estimated cytosolic fraction as a function of time; the decay of the readout following treatment with the MEK inhibitor, U0126, is also shown. (F) Confocal image of a representative cell expressing ERKKTR-Clover, fixed after PDGF stimulation, confirming nearly complete translocation.

of ERKKTR whenever the biosensor is not engaged in actively transported complexes.

The model was globally fit to the four acquired live-cell imaging data sets, together with archival, biochemical data reported in our previous study (Ahmed *et al.*, 2014). Fitting was performed as consistent as possible with the prior study; the key difference here is that the ERKKTR response, quantified as the fraction of the biosensor mass in the cytosol, was fit by the model directly (i.e., without alignment). An ensemble of 5000 sets of parameter values was thus identified, and the ensemble-averaged output successfully captures the distinct features of the measured kinetics (Figure 3, D–M). In parallel, fitting was also performed without the ERKKTR data or ERKKTR-specific model equations. The distributions of parameter vales for the two ensembles (with and without ERKKTR) are shown in Supplemental Figure S4.

Relative to the previously published analysis, the inclusion of ERKKTR data as a fitting constraint yielded more precise predictions of ERK dynamics across the ensemble of parameter sets. This was assessed in terms of predicted substrate buffering strengths (ratio of the total substrate concentration to the corresponding K_m) in the cytosol and nucleus and the fractions of ERK in various phosphorylation and localization states (Figure 4). Here the prediction is that substrate buffering in the cytosol is consistently strong and somewhat stronger than that in the nucleus. In contrast, for the ensemble generated without ERKKTR, a similar goodness of fit could be achieved with weak substrate buffering in the cytosol, provided that substrate buffering in the nucleus was strong (Supplemental Figure S5), in agreement with the ensemble generated previously (Ahmed *et al.*, 2014). The ensemble with ERKKTR, in addition to predicting more narrowly distributed substrate buffering strengths, has narrower distributions of parameters related to ERK phosphorylation/dephosphorylation and translocation (Supplemental Figure S4).

Model predictions can explain the distinct kinetics of ERKKTR translocation relative to ERK kinase activity

Just as the ERKKTR kinetics help refine the model-guided interpretation of ERK dynamics, the model can offer interpretations of the ERKKTR response. Analysis of the biosensor-specific rate constants for the parameter set with the lowest weighted error (Figure 5A) and ensemble-averaged, predicted kinetics (Figure 5B) yields the following narrative for the poststimulation dynamics. Given that most of the ERKKTR in the cell is cytosolic, and availability of active ERK in the nucleus is delayed, the initial phosphorylation of ERKKTR occurs in the cytosol and on the NES (*Sup* in the model). This form can still be imported to the nucleus (*Rup* in the model), but it is rapidly exported, and thus there is a net flux of ERKKTR from the nucleus to the cytosol, even in the absence of freely available ERK activity in the nucleus. As active ERK gradually becomes available in the nucleus, more of the ERKKTR becomes fully phosphorylated there (*Rpp* in the model) and exported to the cytosol (*Spp* in the model). Eventually, almost all of the ERKKTR is cytosolic. Although the unphosphorylated *Suu* species persists and continues to be imported to the nucleus, it is rapidly phosphorylated and exported upon arrival, and ERKKTR awaiting release from ECs is predicted to be a major fraction of the cytosolic pool (Figure 5B).

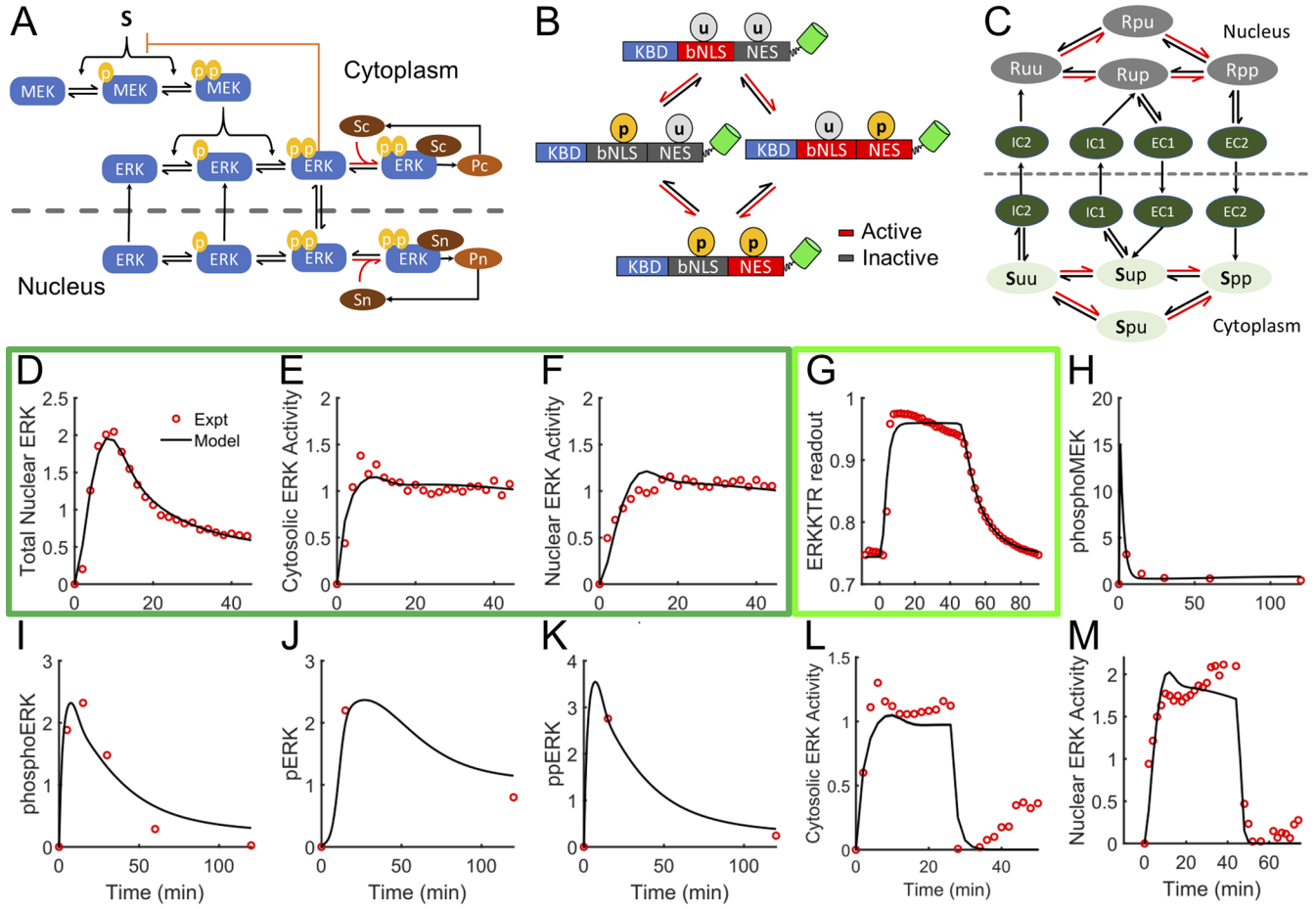

FIGURE 3: Data-driven kinetic modeling of ERK activation, including ERKKTR data and dynamics. (A) Schematic of ERK phosphorylation, localization, and activity, adapted from Ahmed *et al.* (2014). (B) Phosphorylation network of ERKKTR biosensor. The red arrows signify phosphorylation reactions catalyzed by ERK. Phosphorylation neutralizes the bNLS, whereas it activates the NES. (C) Nucleocytoplasmic shuttling model of ERKKTR. Nuclear (*Rxx*) and cytosolic (*Sxx*) phospho-forms follow the notation shown in B; for example, *Rpu* is the fraction of ERKKTR that is free in the nucleus with its bNLS phosphorylated and its NES unphosphorylated. IC1/2 refer to ICs that form when the bNLS is not phosphorylated; EC1/2 refer to ECs that form when the NES is phosphorylated. As in B, the red arrows signify phosphorylation reactions catalyzed by ERK. (D–M) Aligned model fits of the data used to acquire good-fitting parameter sets. The red dots show the experimental means, and the solid black line shows the mean ± 95% confidence intervals for the parameter set ensemble ($n = 5000$). The dark green box encloses new live-cell imaging data from Figure 1B-D, which replicated previous data presented in Ahmed *et al.* (2014). The light green box indicates the newly acquired ERKKTR data. The rest of the time courses are archival data from Ahmed *et al.* (2014).

The results likewise offer an interpretation of the relatively slow decay of the ERKKTR readout following the subsequent inhibition of MEK and rapid cessation of ERKKTR phosphorylation. In the model, ERKKTR is protected from dephosphorylation while engaged in import and ECs, which collectively act as a buffer. Consequently, as ERKKTR is dephosphorylated, there is an accumulation and retention of the forms that are not actively transported (*Spu* and *Rpu* in the model) (Figure 5B). These effects can explain the sluggish reset of the biosensor's localization.

DISCUSSION

Live-cell fluorescence microscopy is a powerful and prevalent experimental tool in cell biology. To obtain quantitative insights from a biosensor readout, it is important to acquire and analyze the image data carefully; however, even a careful measurement can be misleading or misinterpreted if the dynamics intrinsic to the biosensor affect the measured response in a way that does not reflect, or perturbs, the native dynamics (Haugh, 2012). The KTR biosensors for ERK1/2, JNK, and p38 are synthetic substrates designed using binding domains from established substrates of the respective MAPKs, together with sequences that affect translocation of the biosensor upon phosphorylation (Regot *et al.*, 2014). They have been widely adopted because the readouts report endogenous kinase activity with greater sensitivity/signal-to-noise than FRET-based activity reporters (Kudo *et al.*, 2018). In this study, we have compared the kinetics of ERK1/2 signaling as reported by ERKKTR to those reported by compartment-specific activity reporters and by the overall localization of FP-tagged ERK2. We found that the ERKKTR, though suitable and in some ways superior as an indicator of ERK activity, does not generally reflect the kinetics of either cytosolic or nuclear ERK1/2 activity nor does it approximate a weighted sum of the two. This is apparent from the initial lag of the ERKKTR response, its slow adaptation, and its sluggish decay following MEK inhibition. For certain other experimental contexts, particularly when fine temporal resolution of the dynamics is less important, the ERKKTR may be well suited for quantitative studies. For example, ERKKTR has been used

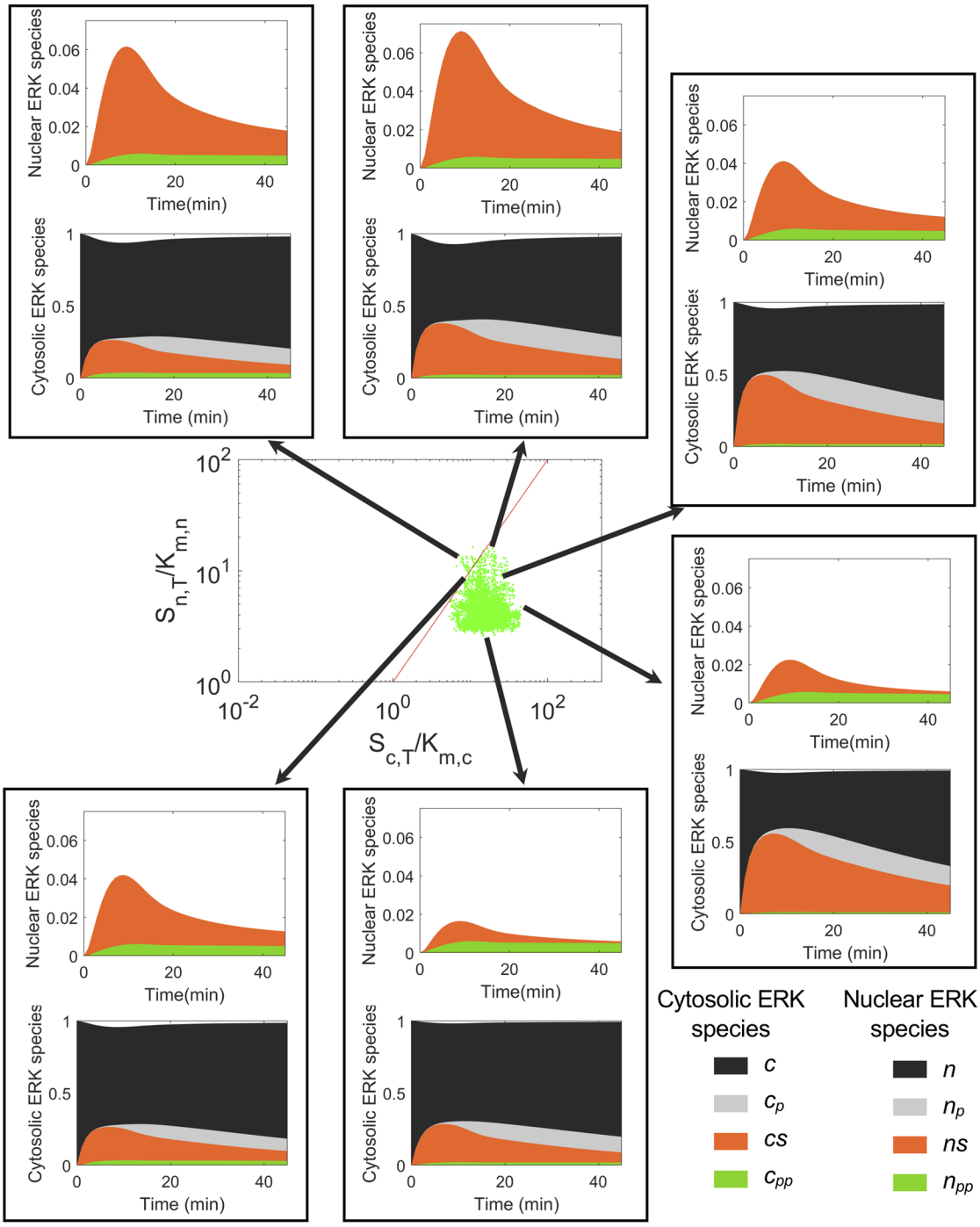

FIGURE 4: Inclusion of ERKKTR data further constrains predictions concerning the buffering strengths of ERK-substrate interactions in the cytosol and nucleus. The substrate buffering strength (total concentration of the substrate divided by the corresponding K_m K_M) in the cytosol and nucleus are plotted for each parameter set in the ensemble (center plot). The breakdowns of ERK species in the cytosol and nucleus are shown for 6 selected parameter sets (connected by the arrows). The model variables c/n, c_p/n_p, c_{pp}/n_{pp}, and cs/ns represent the cytosolic/nuclear unphosphorylated, monophosphorylated, diphosphorylated, and substrate-bound ERK. The freely available, active ERK species, c_{pp} and n_{pp}, are inputs to the ERKKTR submodel.

to monitor ERK activity during developmental and homeostatic processes in model organisms, including *Caenorhabditis elegans* (de la Cova *et al.*, 2017), zebrafish (Mayr *et al.*, 2018), *Drosophila* (Yuen *et al.*, 2022), and mouse (Okuda *et al.*, 2021).

An updated mathematical model was able to fit the ERKKTR and other biosensor responses thus reconciling the disparate kinetics. The present model has many more parameters to account for the dynamics specific to ERKKTR, yet the additional data and model complexity yielded a more constrained prediction of ERK dynamics. This analysis demonstrates the utility of ERKKTR when combined with other ERK biosensors. The modeling also offers an interpretation of why ERKKTR responds as it does to stimulation. We initially

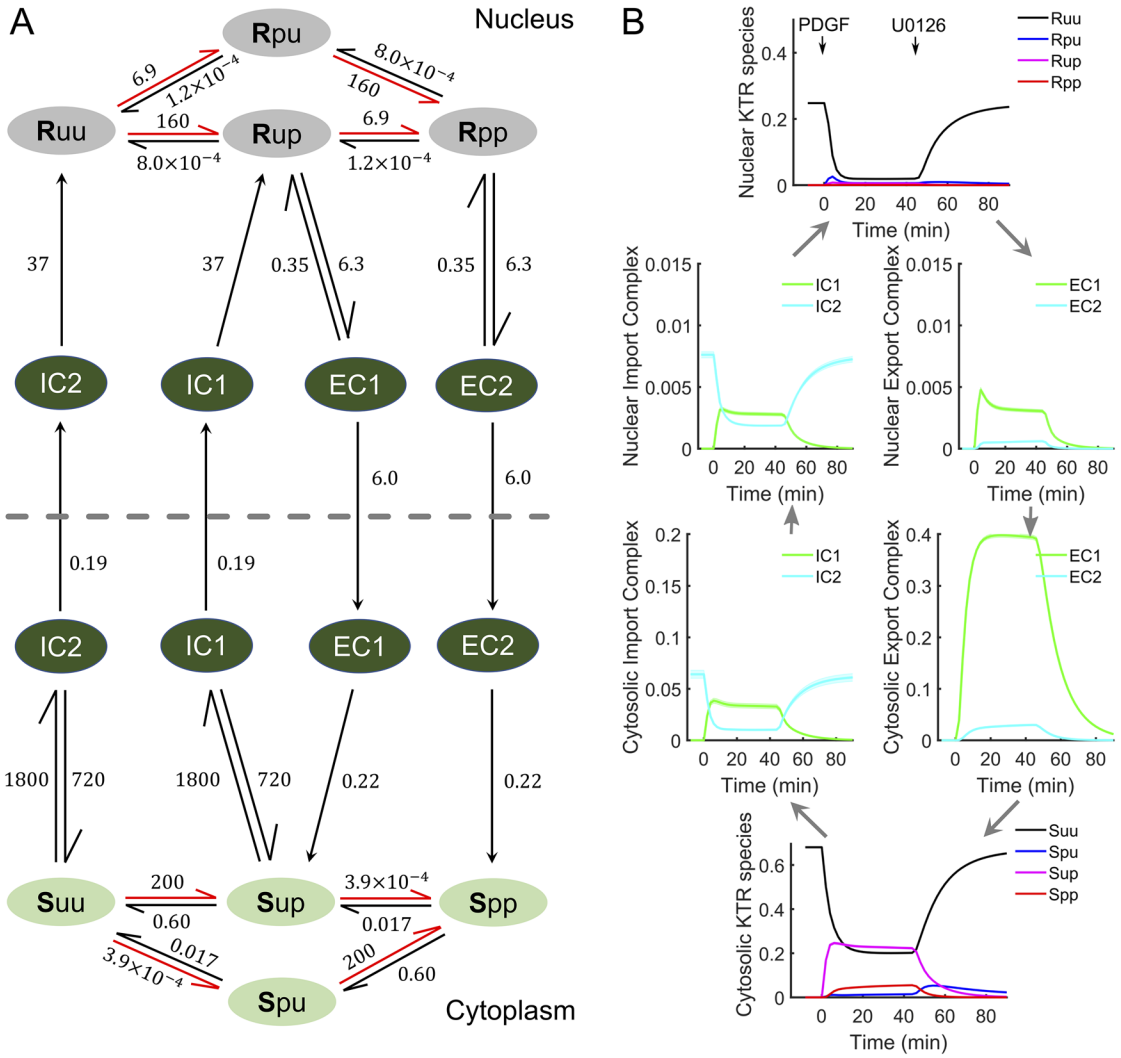

FIGURE 5: Modeling-based interpretation of ERKKTR dynamics. (A) ERKKTR submodel, as depicted in Figure 3C, showing the values of rate constants (min^{-1}) for the parameter set with the lowest weighted error in the ensemble. For the phosphorylation reactions (red arrows), the rate laws include the time-dependent fractions of ERK that are free and active in the nucleus (n_{pp}) or cytosol (c_{pp}). Not shown: passive shuttling via diffusion through nuclear pores. (B) Ensemble-averaged kinetics of all the ERKKTR species (mean ± 95% confidence intervals, $n = 5000$). The gray arrows signify the cycle of ERKKTR export and import.

wondered how the sluggish accumulation of nuclear, active ERK available to phosphorylate ERKKTR might drive the observed kinetics of the biosensor's translocation. The slow kinetics of the nuclear activity could explain the lag of the response but not its rapid increase thereafter. Hence a key insight and modeling constraint was our experimental determination that ERKKTR is, by mass, predominantly cytosolic even prior to stimulation in our cells. Accordingly, the modeling suggests that substantial phosphorylation of cytosolic ERKKTR occurs before active ERK is available to phosphorylate nuclear ERKKTR; however, nuclear import and export of ERKKTR phosphorylated only on the NES might frustrate the translocation process initially. The modeling also suggests why the full reset of the ERKKTR localization following MEK inhibition takes much longer than the decay of ERK activity. Again, this can largely be attributed to the import/export mechanisms, which could buffer dephosphorylation of the biosensor and drive accumulation of ERKKTR phosphorylated only on the bNLS, which translocates via passive transport only.

The present analysis and insights could inform the design of new KTR biosensors. We contend that a more ideal KTR should be almost entirely in one compartment when unphosphorylated; then, upon phosphorylation, there is net translocation of the KTR to the other compartment. A KTR that transitions from almost entirely nuclear (or cytosolic) to partially cytosolic (or nuclear) could offer an excellent readout of nuclear (or cytosolic) kinase activity. Instead, ERKKTR transitions from mostly cytosolic to almost entirely cytosolic, with kinetics that are apparently frustrated by the biosensor-specific dynamics. One strategy is to identify a single localization sequence—either a NLS or NES—that is strong in the absence of phosphorylation but then neutralized upon phosphorylation. In that scenario, translocation of the phosphorylated KTR would be via passive transport, which would be rapid enough to report changes in kinase activity that occur on the timescale of ~5 min or slower. Dephosphorylation of the KTR in both compartments would also need to be sufficiently fast. This strategy is simple in concept, but achieving it is another matter. The rational design or directed evolution of translocation-based reporters that faithfully track compartment-specific kinase activities presents an exciting protein engineering challenge.

MATERIALS AND METHODS

Reagents and plasmids

PDGF was purchased from Peprotech (Rocky Hill, NJ) and U0126 was purchased from Millipore Sigma (Burlington, MA). Human fibronectin was purchased from Fisher Scientific (#CB-40008) (Hampton, NH). All other plasmids were obtained from Addgene: GFP-ERK2 (#37145) (Yung *et al.*, 2001); cyto-EKAR (#18679) and nuc-EKAR (#18681) (Harvey *et al.*, 2008); ERKKTRs pLenti-PGK-Blast-ERKKTR-mRuby2 (#90231) and pLentiCMV Puro DEST ERKKTR-Clover (# 59150) (Regot *et al.*, 2014).

Cell culture

NIH 3T3 mouse fibroblasts were acquired from American Type Culture Collection (Manassas, VA). The cells were cultured in DMEM supplemented with 10% fetal bovine serum and 1% penicillin/streptomycin/glutamine solution (PSG). All tissue culture reagents were purchased from Thermo Fisher Scientific/Invitrogen (Carlsbad, CA). For transient transfection, ~200,000 cells were plated per 35-mm dish 24 h prior. Lipofectamine 3000 and P3000 reagents or Lipofectamine and Plus reagents were used according to the manufacturer's protocol; 24 h after transfection, 50,000 cells were replated on a fibronectin-coated (10 µg/ml coating concentration) 35-mm glass-bottom dish (MatTek) with normal growth medium. After allowing the cells to spread for 2–3 h, the subconfluent cells were lightly serum-starved for 4 h prior to imaging. The imaging buffer composition was 20 mM HEPES, 125 mM NaCl, 5 mM KCl, 1.5 mM $MgCl_2$, 1.5 mM $CaCl_2$, 10 mM glucose, and 2 mg/ml fatty acid-free bovine serum albumin, pH 7.4, supplemented with 1% PSG. The imaging chamber is maintained at 37°C, and mineral oil is layered on top of the imaging buffer to prevent evaporation during the experiment. Cells were imaged in a quiescent state for 20–30 min before the addition of 1 nM PDGF. These steps closely followed the protocol used in our previous study (Ahmed *et al.*, 2014).

Microscopy and image processing

Sequential images were acquired by epifluorescence using a modified Axioskop 2 FS microscope equipped with a 40× 0.8 NA Achroplan water-dipping objective (Carl Zeiss) and charge-coupled device camera (ORCA ER; Hamamatsu Photonics). A 50 W mercury lamp was used to excite Cerulean, Clover/EGFP, and mCherry fluorophores using 436/20-, 480/20-, and 572/20-nm excitation band-pass filters, respectively. Band-pass emission filters were 480/40 and 535/30 nm for Cerulean and Venus, respectively (FRET reporters); 525/50 nm for Clover and EGFP constructs; and 645/75 nm for mCherry fluorophores. The excitation and emission filters were purchased from Chroma Technology Corp. MetaMorph software (Universal Imaging) was used for automatic image acquisition. For image processing, the binary cell mask of individual cells was generated using a custom MATLAB code. The binary cell mask was used to track the individual cells using the lineage mapper's MATLAB plugin (Chalfoun *et al.*, 2016). For ERKKTR C/N ratio or FP-tagged ERK1/2 nuclear translocation measurement, the nuclear mask was generated using the Microscopy Image Browser (Belevich *et al.*, 2016). Finally, a custom MATLAB script was written to incorporate the lineage mapper tracking information and nuclear mask information needed to calculate the fractions of ERKKTR mass in the cytosol and nucleus or the mean nuclear over total intensity ratio of FP-ERK2 for individual cells. For processing the EKAR reporter data, the lineage mapper tracking information was used to track and calculate the mean intensity ratio of YFP/CFP from the background-subtracted cellular regions. The FP-ERK1/2 and EKAR experimental data were normalized to the initial value.

Confocal fluorescence microscopy of fixed cells was performed using a Nikon A1R confocal microscope (Nikon Instruments) equipped with a 40× oil immersion objective and 488-nm laser line. The acquired ND2 z-stacks were imported and XZ and YZ projections of individuals cells were obtained using FIJI analysis software (Schindelin *et al.*, 2012).

Kinetic modeling and ensemble-based data fitting

The model equations that account for the phosphorylation, localization, and activity states of ERK1/2 (Ahmed *et al.*, 2014) were used without modification to calculate the free ERK activities in the cytosol and nucleus as a function of time following PDGF stimulation and subsequent MEK inhibition. These two outputs are passed to a new submodel of ERKKTR dynamics represented by the reaction network shown in Figure 3C. In this network, all transitions follow (pseudo) first-order/unimolecular kinetics, except for the reactions in which ERKKTR is phosphorylated by ERK reactions; for those, bimolecular kinetics are assumed with rates proportional to the free ERK activity in the compartment. In addition to the transitions shown in the network, we included passive, diffusion-based transport of free ERKKTR species (those not in import/ECs) through nuclear pore complexes (NPCs). For this, the net rate of nuclear influx (molecules/time) via passive diffusion, per NPC, is given by

$$Rate = p\left(C_{cyt} - C_{nuc}\right)$$

where C_{cyt} and C_{nuc} are the concentrations of the protein species in the cytosol and nucleus, respectively. Bizzarri *et al.* (2012) quantified the passive nucleocytoplasmic exchange in fibroblasts by photobleaching the nucleus and monitoring the kinetics of recovery (Bizzarri *et al.*, 2012). In terms of the rate developed above, the recovery experiment is characterized by the following differential equation,

$$\frac{dC_{nuc}}{dt} = \frac{pN_{NPC}\left(C_{cyt} - C_{nuc}\right)}{V_{nuc}};\ C_{nuc}(0) \approx 0$$

where N_{NPC} is the number of NPCs spanning the nuclear membrane, and V_{nuc} is the volume of the nucleoplasm. Bizzarri *et al.* (2012) estimated, for exchange of EGFP (27-kDa) in a mammalian cell line, a rate constant of

$$\frac{p_{EGFP}N_{NPC}}{V_{nuc}} = 1.0\ \text{min}^{-1}$$

To adjust for the molecular weight of ERKKTR (35-kDa), we follow the correlation of Timney *et al.* (2016), who showed an approximately inverse-cubic dependence of p on molecular weight (Timney *et al.*, 2016), yielding an estimated rate constant for passive nuclear import of free ERKKTR species,

$$k_{PI} = \frac{p_{ERKKTR}N_{NPC}}{V_{nuc}} = \left(\frac{27}{35}\right)^3 (1.0) = 0.46\ \text{min}^{-1}$$

ERKKTR species variables are formulated as fractions of total cellular ERKKTR, and so, for example, the rate of unphosphorylated ERKKTR import by passive diffusion (fraction of total ERKKTR/time) is given by

$$Rate = p_{ERKKTR}N_{NPC}\left(\frac{Suu}{V_{cyt}} - \frac{Ruu}{V_{nuc}}\right) = k_{PI}\left[\left(\frac{V_{nuc}}{V_{cyt}}\right)Suu - Ruu\right]$$

As explained in the text, we estimated for our cells that the nucleus is, on average, approximately 16% of the accessible cellular volume; hence for the model calculations, we fixed the value of

$$\frac{V_{nuc}}{V_{cyt}} = \frac{0.16}{0.84} = 0.19$$

A full specification of model variables, conservation equations, and parameters is provided in Supplemental Text S1.

Ensemble parameter fitting to the combined ERK/ERKKTR model was performed using a Monte Carlo scheme, implemented in MATLAB. The pertinent MATLAB and other files are included in the Supplemental Material. The scheme was described in detail previously (Ahmed *et al*., 2014), with necessary modifications. As before, in each iteration, nuclear ERK2 and EKAR imaging data and the biochemical data were aligned with the corresponding model outputs/observables, and the sum of squared deviations (SSD) was calculated for each time course. These individual SSDs were weighted as before (with weighting factors ranging from 1 to 10) and summed in the cumulative SSD. The ERKKTR readout (fraction in the cytosol) was neither normalized nor aligned with the model output. Because the individual SSD of the ERKKTR fit is uniquely sensitive to the ERKKTR-specific parameters, its weighting factor in the cumulative SSD needed to be much higher than the others (150) to constrain acceptable fits of the combined model. The algorithm was run until the running average of the cumulative SSD had converged to an acceptable degree, with more than 10^5 parameter sets stored. The final ensemble of parameter sets was selected by 1) imposing conservative individual SSD cutoffs; and then 2) selecting among those the 5000 parameter sets with the lowest cumulative SSD.

Estimation of fold increase in nuclear import of unphosphorylated ERKKTR due to the bNLS

The steady-state conservation of unphosphorylated ERKKTR in the cytosol (as a fraction of total ERKKTR in the cell), in the absence ERK activity, may be written as follows.

$$\frac{dSuu}{dt} = -R_{bNLS} - k_{PI}\left[\left(\frac{V_{nuc}}{V_{cyt}}\right)Suu - Ruu\right] = 0$$

where R_{bNLS} is the portion of the import rate attributed to the active import. Using this equation, the fold increase in import rate relative to passive import is calculated as

$$\frac{R_{bNLS} + k_{PI}\left(\frac{V_{nuc}}{V_{cyt}}\right)Suu}{k_{PI}\left(\frac{V_{nuc}}{V_{cyt}}\right)Suu} = \frac{k_{PI}Ruu}{k_{PI}\left(\frac{V_{nuc}}{V_{cyt}}\right)Suu} = \left(\frac{V_{cyt}}{V_{nuc}}\right)\frac{Ruu}{Suu}$$

The approximate estimate we give in the text neglects the fraction of ERKKTR in the IC. Incorporating our experimental estimates,

$$\left(\frac{V_{cyt}}{V_{nuc}}\right)\frac{Ruu}{Suu} \approx \left(\frac{0.86}{0.14}\right)\frac{0.25}{0.75} = 2.0$$

ACKNOWLEDGMENTS

We thank the laboratory of Albert Keung, especially Ryan Tam, for assistance with confocal microscopy. Research reported in this publication was supported by the National Institute of General Medical Sciences of the National Institutes of Health, under award no. R01-GM141691, and by a UNC Lineberger Developmental Grant from the University Cancer Research Fund. The content is solely the responsibility of the authors and does not necessarily represent the official views of the National Institutes of Health.

REFERENCES

Ahmed S, Grant KG, Edwards LE, Rahman A, Cirit M, Goshe MB, Haugh JM (2014). Data-driven modeling reconciles kinetics of ERK phosphorylation, localization, and activity states. Mol Syst Biol 10, 718.

Belevich I, Joensuu M, Kumar D, Vihinen H, Jokitalo E (2016). Microscopy Image Browser: A platform for segmentation and analysis of multidimensional datasets. PLoS Biol 14, e1002340.

Bizzarri R, Cardarelli F, Serresi M, Beltram F (2012). Fluorescence recovery after photobleaching reveals the biochemistry of nucleocytoplasmic exchange. Anal Bioanal Chem 403, 2339–2351.

Chalfoun J, Majurski M, Dima A, Halter M, Bhadriraju K, Brady M (2016). Lineage mapper: A versatile cell and particle tracker. Sci Rep 6, 36984.

Chang L, Karin M (2001). Mammalian MAP kinase signalling cascades. Nature 410, 37–40.

Chavez-Abiega S, Goedhart J, Bruggeman FJ (2019). Physical biology of GPCR signalling dynamics inferred from fluorescence spectroscopy and imaging. Curr Opin Struct Biol 55, 204–211.

Cole CN, Hammell CM (1998). Nucleocytoplasmic transport: driving and directing transport. Curr Biol 8, R368–R372.

de la Cova C, Townley R, Regot S, Greenwald I (2017). A real-time biosensor for ERK activity reveals signaling dynamics during C. elegans cell fate specification. Dev Cell 42, 542–553.

Ebisuya M, Kondoh K, Nishida E (2005). The duration, magnitude and compartmentalization of ERK MAP kinase activity: mechanisms for providing signaling specificity. J Cell Sci 118, 2997–3002.

Freitas N, Cunha C (2009). Mechanisms and signals for the nuclear import of proteins. Curr Genomics 10, 550.

Gaits F, Hahn K (2003). Shedding light on cell signaling: interpretation of FRET biosensors. Science's STKE 2003, pe3–pe3.

Gama-Carvalho M, Carmo-Fonseca M (2001). The rules and roles of nucleocytoplasmic shuttling proteins. FEBS Lett 498, 157–163.

Garrington TP, Johnson GL (1999). Organization and regulation of mitogen-activated protein kinase signaling pathways. Curr Opin Cell Biol 11, 211–218.

Hahn K, Toutchkine A (2002). Live-cell fluorescent biosensors for activated signaling proteins. Curr Opin Cell Biol 14, 167–172.

Harvey CD, Ehrhardt AG, Cellurale C, Zhong H, Yasuda R, Davis RJ, Svoboda K (2008). A genetically encoded fluorescent sensor of ERK activity. Proc Natl Acad Sci USA 105, 19264–19269.

Haugh JM (2012). Live-cell fluorescence microscopy with molecular biosensors: what are we really measuring? Biophys J 102, 2003–2011.

Kim Y, Andreu MJ, Lim B, Chung K, Terayama M, Jiménez G, Berg CA, Lu H, Shvartsman SY (2011). Gene regulation by MAPK substrate competition. Dev Cell 20, 880–887.

Kim YH, Han M-E, Oh S-O (2017). The molecular mechanism for nuclear transport and its application. Anat Cell Biol 50, 77–85.

Kohno M, Pouyssegur J (2006). Targeting the ERK signaling pathway in cancer therapy. Ann Med 38, 200–211.

Kudo T, Jekni S, Macklin DN, Akhter S, Hughey JJ, Regot S, Covert MW (2018). Live-cell measurements of kinase activity in single cells using translocation reporters. Nat Protoc 13, 155–169.

Kuersten S, Ohno M, Mattaj IW (2001). Nucleocytoplasmic transport: Ran, beta and beyond. Trends Cell Biol 11, 497–503.

Lee N, Lee JW, Kang GY, Park SH, Kim KP (2019). Quantification of the dynamic phosphorylation process of ERK using stable isotope dilution selective reaction monitoring mass spectrometry. Proteomics 19, 1900086.

Mayr V, Sturtzel C, Stadler M, Grissenberger S, Distel M (2018). Fast dynamic in vivo monitoring of Erk activity at single cell resolution in DREKA zebrafish. Front Cell Dev Biol 6, 111.

McCubrey JA, Steelman LS, Chappell WH, Abrams SL, Wong EW, Chang F, Lehmann B, Terrian DM, Milella M, Tafuri A (2007). Roles of the Raf/MEK/ERK pathway in cell growth, malignant transformation and drug resistance. Biochim Biophys Acta-Mol Cell Res 1773, 1263–1284.

Mebratu Y, Tesfaigzi Y (2009). How ERK1/2 activation controls cell proliferation and cell death: Is subcellular localization the answer? Cell Cycle 8, 1168–1175.

Meyer T, Teruel MN (2003). Fluorescence imaging of signaling networks. Trends Cell Biol 13, 101–106.
Okuda KS, Keyser MS, Gurevich DB, Sturtzel C, Mason EA, Paterson S, Chen H, Scott M, Condon ND, Martin P (2021). Live-imaging of endothelial Erk activity reveals dynamic and sequential signalling events during regenerative angiogenesis. eLife 10, e62196.
Pemberton LF, Paschal BM (2005). Mechanisms of receptor-mediated nuclear import and nuclear export. Traffic 6, 187–198.
Regot S, Hughey JJ, Bajar BT, Carrasco S, Covert MW (2014). High-sensitivity measurements of multiple kinase activities in live single cells. Cell 157, 1724–1734.
Roberts PJ, Der CJ (2007). Targeting the Raf-MEK-ERK mitogen-activated protein kinase cascade for the treatment of cancer. Oncogene 26, 3291–3310.
Sasagawa S, Ozaki Y-iFujita K, Kuroda S (2005). Prediction and validation of the distinct dynamics of transient and sustained ERK activation. Nat Cell Biol 7, 365–373.
Schevzov G, Kee AJ, Wang B, Sequeira VB, Hook J, Coombes JD, Lucas CA, Stehn JR, Musgrove EA, Cretu A (2015). Regulation of cell proliferation by ERK and signal-dependent nuclear translocation of ERK is dependent on Tm5NM1-containing actin filaments. Mol Biol Cell 26, 2475–2490.
Schindelin J, Arganda-Carreras I, Frise E, Kaynig V, Longair M, Pietzsch T, Preibisch S, Rueden C, Saalfeld S, Schmid B (2012). Fiji: an open-source platform for biological-image analysis. Nat Methods 9, 676–682.
Seger R, Krebs EG (1995). The MAPK signaling cascade. FASEB J 9, 726–735.
Shankaran H, Ippolito DL, Chrisler WB, Resat H, Bollinger N, Opresko LK, Wiley HS (2009). Rapid and sustained nuclear–cytoplasmic ERK oscillations induced by epidermal growth factor. Mol Syst Biol 5, 332.
Timney BL, Raveh B, Mironska R, Trivedi JM, Kim SJ, Russel D, Wente SR, Sali A, Rout MP (2016). Simple rules for passive diffusion through the nuclear pore complex. J Cell Biol 215, 57–76.
Yuen AC, Prasad AR, Fernandes VM, Amoyel M (2022). A kinase translocation reporter reveals real-time dynamics of ERK activity in Drosophila. Biol Open 11, bio059364.
Yung Y, Yao Z, Aebersold DM, Hanoch T, Seger R (2001). Altered regulation of ERK1b by MEK1 and PTP-SL and modified Elk1 phosphorylation by ERK1b are caused by abrogation of the regulatory C-terminal sequence of ERKs. J Biol Chem 276, 35280–35289.
Zacharias DA, Baird GS, Tsien RY (2000). Recent advances in technology for measuring and manipulating cell signals. Curr Opin Neurobiol 10, 416–421.
Zhang W, Liu HT (2002). MAPK signal pathways in the regulation of cell proliferation in mammalian cells. Cell Res 12, 9–18.